lubricants

MDPI

Article

The Influences of Surface Texture Topography and Orientation on Point-Contact Mixed Lubrication

Chengjiao Yu [1,2,*], Rui Cheng [2], Hongwei Zhang [2], Chicheng Ma [1,2,*] and Shuangcheng Yu [3,4]

[1] State Key Laboratory of Reliability and Intelligence of Electrical Equipment, Hebei University of Technology, Tianjin 300401, China
[2] School of Mechanical Engineering, Hebei University of Technology, Tianjin 300401, China; 16622893868@163.com (R.C.); zhw8887@126.com (H.Z.)
[3] Sunmetals Products of America LLC, Dallas, TX 75237, USA; shaun.yu@sunmetalspro.com
[4] Xingyi Metalworking Technology (Zhejiang) Co., Ltd., Jiaxing 314408, China
* Correspondence: yucj@hebut.edu.cn (C.Y.); machch@hebut.edu.cn (C.M.)

Abstract

Surface topography plays a critical role in determining the tribological performance of engineering surfaces. This study systematically investigates the lubrication film characteristics of bump array surfaces (isotropic and anisotropic), groove surfaces, and herringbone surfaces through point-contact elastohydrodynamic lubrication (EHL) analyses. Numerical simulations were conducted to evaluate the influences of surface topographical parameters on the lubrication performance, which is quantified by average film thickness and contact load ratio. The results indicate that transverse textures lead to thicker average film as compared with longitudinal textures. This is mainly because the transverse textures can generate more effective hydrodynamic pressures from the oil film behind the ridges due to micro-EHL. By analyzing the topographical parameters and their impacts on the average film thickness and contact load ratio, this study provides practical guidance for designing surface topographies that optimize average film thickness, applicable to a wide range of tribological systems.

Keywords: surface texture; lubrication film; contact load ratio; EHL; mixed lubrication

check for updates

Received: 17 June 2025
Revised: 3 September 2025
Accepted: 10 September 2025
Published: 12 September 2025

Citation: Yu, C.; Cheng, R.; Zhang, H.; Ma, C.; Yu, S. The Influences of Surface Texture Topography and Orientation on Point-Contact Mixed Lubrication. *Lubricants* **2025**, *13*, 409. https://doi.org/10.3390/lubricants13090409

Copyright: © 2025 by the authors. Licensee MDPI, Basel, Switzerland. This article is an open access article distributed under the terms and conditions of the Creative Commons Attribution (CC BY) license (https://creativecommons.org/licenses/by/4.0/).

1. Introduction

In actual machining processes of components such as bearings, perfectly smooth surfaces are rarely achievable. Instead, surface topographies with certain roughness levels are commonly observed. According to relevant literature [1–3], the surface roughness (Ra) of machined parts typically ranges from 0.01 μm to 2 μm, depending on the processing method and material. Surface topography plays a crucial role in the lubrication by influencing lubricant retention and load distribution. Understanding and controlling the surface topography through surface roughness or surface texture is essential for designing and optimizing tribological systems for reliable and efficient operation [4]. These improvements can lead to extended equipment lifespan, reduced energy consumption, and lower maintenance costs in various applications [5,6], including automotive engines, industrial machinery, and aerospace components. Scientists and engineers continue to explore the benefits of surface texturing research focuses on understanding the mechanisms by which surface textures enhance lubrication, such as facilitating the retention of lubricant within surface features to withstand high shear forces and provide adequate film thickness to prevent metal-to-metal contact.

Significant amounts of studies on the influences of isotropic structures on their lubrication behaviors were reported by using elastohydrodynamic lubrication (EHL) simulation and experiments. Early studies systematically explored the behavior patterns of asperities in EHL. Kaneta and Cameron [7] discovered the modulation effect of surface asperities on the oil film pressure. Choo et al. [8] revealed the correlation between surface topography and film thickness through three-dimensional roughness measurements. Zheng et al. [9] fabricated regularly arranged circular dimples, which significantly improved the friction and wear behavior of graphite under water lubrication. Wang et al. [10] prepared triangular and hexagonal textures that enhanced the wettability and lubrication performance of silicon nitride ceramics. Chen et al. [11] employed a two-step laser process to construct micro/nano hierarchical textures on PS-SiC ceramics, substantially improving their lubrication and anti-wear capabilities. Jiang et al. [12] reported that surface textures could induce synergistic deformation at soft contact interfaces and enhance fluid film support, thus reducing frictional resistance. Wu et al. [13] found that appropriate surface texturing can significantly enhance oil film load-carrying capacity and reduce the friction coefficient. The mixed lubrication experiments conducted by Guangteng et al. [14] provided crucial insights for the optimal design of surfaces. These studies indicate that under rolling and sliding conditions, the film thickness and surface deformation levels vary for the same type of surface, with sliding conditions significantly influencing surface topography deformation.

Researchers have also conducted studies on anisotropic periodic surfaces, such as longitudinally or transversely grooved surfaces. The averaging flow model established by Patir and Cheng [15] laid a theoretical foundation for the analysis of grooved surfaces. Venner and Lubrecht [16] has revealed the differences in the evolution of lubricant films for transverse textures through numerical simulations. Wedeven and Cusano [17] experimentally observed that both transversely and longitudinally anisotropic textures produce film thickness values smaller than those of smooth surfaces. However, transversely anisotropic textures cause less reduction in film thickness compared to longitudinally anisotropic textures. Choo et al. [18,19] experimentally discovered that under mixed lubrication conditions, longitudinally anisotropic textures exhibit more stable and predictable film thickness compared to transversely anisotropic textures. Pei [20] revealed the relationship between sinusoidal groove density and oil film thickness. Wang et al. [21,22] investigated the influence of anisotropy orientation angles relative to the rolling direction on lubrication parameters under both full-film and mixed lubrication regimes. The results demonstrated that among the generated surfaces, transversely anisotropic textures exhibited greater average film thickness than longitudinally anisotropic surfaces. Peng et al. [23], through molecular dynamics simulations, revealed that the geometric characteristics of surface grooves significantly influence the orientation of lubricant molecules and the formation of crystalline bridges, serving as key factors in nanoscale lubrication performance. Studies indicate that under point-contact mixed lubrication conditions, longitudinally anisotropic textures exhibit stability and predictability, while transversely anisotropic textures cause less reduction in film thickness. However, as speed increases and the system transitions to full-film lubrication, the influence of surface topography orientation on film thickness diminishes significantly.

With the advancements in surface processing and fabrication technologies, researchers such as Boidi et al. [24] have compared the frictional responses of dimples and radial curved grooves in EHL, and the directional friction control texture proposed by Lu et al. [25] has provided new ideas for complex motion conditions. By selecting appropriate geometric dimensions and optimizing convergence shapes, these surfaces can significantly reduce surface friction coefficients, increase lubricant film thickness during operation, and extend wear life. However, their research mainly focuses on the friction behavior of specific surface textures, without considering the influence of different parameters of surface textures on

EHL. In fact, different surface processing methods result in diverse surface morphologies. Conducting research on only one type of surface makes it difficult to gain a comprehensive understanding of the overall situation.

Although lubrication analyses have been carried out for various surface topographies, studies that comprehensively evaluate lubrication performance from both oil film thickness and asperity load ratio perspectives in the mixed lubrication regime with different types of surface textures are still limited. This paper aims to systematically investigate the influence of surface topography and anisotropy on lubrication performance by comparing three categories of typical surface structures, i.e., bump array surfaces, grooved surfaces, and herringbone surfaces. Such in-depth understanding is expected to provide valuable insights for the surface design of industrial applications, such as bearings and gears, to improve lubrication film.

2. Methods

2.1. Surface Generation

Surfaces with herringbone: The herringbone structure, as shown in Figure 1a, can be numerically generated by the following equation [26]:

$$Z(x,y) = A\cos[k_g * x + k_j a_j \cos(k_j * y)] \quad (1)$$

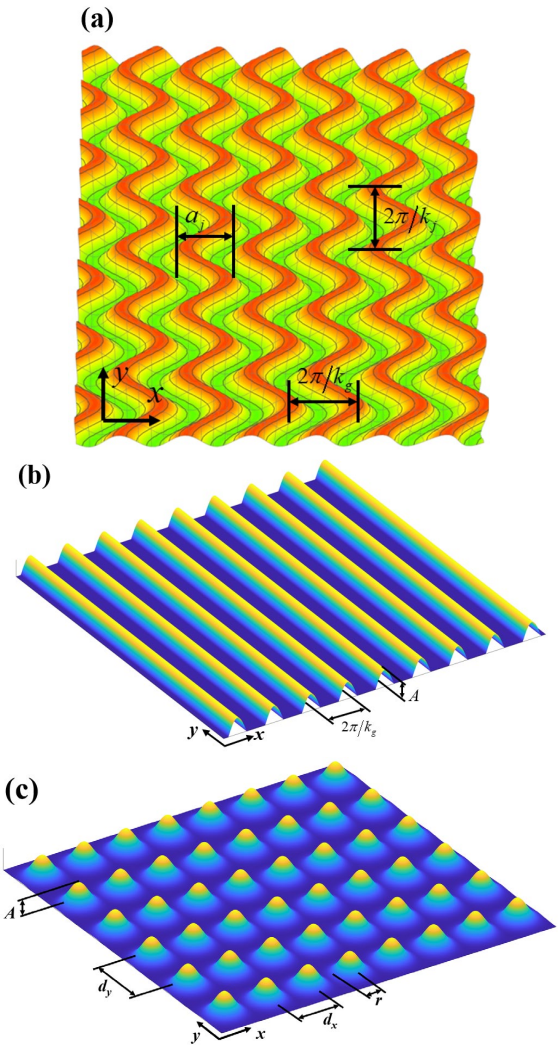


Figure 1. Schematic representations of surface structures and their control parameters. (**a**) herringbone surface, (**b**) groove surface, (**c**) bump array surface (isotropic).

Here, Z is the surface height, and x and y are coordinates in the horizontal along two axis, respectively. A is the amplitude of the function, k_g and k_j are wave numbers in the two orthogonal axes directions, respectively. a_j is the horizontal amplitude of the herringbone folds. The surfaces are designed to have a flat base, which is numerically set by enforcing $Z = 0$ when $Z < 0$ in Equation (1).

Groove surfaces: The groove surfaces are usually defined by extrusion of a cosine function as a cross section along the x or y direction. The cosine function can be accomplished from the herringbone structures by introducing $k_j = 0$ in Equation (1). As shown in Figure 1b, the topography of such groove surfaces is determined by two independent parameters, i.e., wave number k_g and amplitudes A of the cosine function given below:

$$Z(x) = A\cos(k_g * x) \tag{2}$$

The transverse groove surface shown in Figure 1b is generated according to Equation (2). The surfaces are designed to have ridges on a flat base, which is numerically set by enforcing $Z = 0$ when $Z < 0$ in Equation (2).

Surfaces with spherical bumps: The third type of surface in this manuscript is the surface with bump array. The bumps radii are the same, and their centers aligned in an array with fixed spacing in x and y directions. The control parameters are bump heights A, bump radius at the root r, and distances d_x and d_y between the centers of adjacent bumps in the two directions, as shown in Figure 1c.

2.2. EHL Solver

Our three-dimensional (3D) deterministic model for point-contact mixed-EHL problems [27] was used to investigate the lubrication performances of aforementioned surfaces. The point-contact EHL model includes a spherical ball with surface 1, a deformable body with surface 2, and lubrication oil at the interface as shown in Figure 2a on the left side. The EHL solution domain is given on the right side of Figure 2a, the yellow square indicates the size of the EHL solution domain, and the green circle illustrates the Hertzian contact circle. The origin is set to be the center of contact. X_o, X_e are the distances from the left and right boundaries of the computational domain to the origin, respectively. Y_o is the distance from the top and bottom boundaries of the computational domain to the origin, which is chosen to be the same. The solution domain is set as $-1.9 \leq X \leq 1.1$ and $-1.5 \leq Y \leq 1.5$; this size of the solution domain has been widely used to solve EHL problems [28,29]. Here, X and Y indicate the dimensionless coordinates in x and y directions which are normalized by Hertzian contact radius r_a. The rough surfaces are directly digitized in the deterministic model, in which two arbitrary rough surfaces can run through the EHL conjunction at any rolling and relative sliding velocities. Here, to make it simple, a smooth surface 1 and a textured surface 2 are utilized, as demonstrated in Figure 2b, and both surfaces move at the same velocity, maintaining a state of pure rolling motion. The rolling direction is set to be consistent with the x-coordinate for the whole research. It is important to note that the average film thickness, h_a, is selected to characterize the overall performance of the lubricant film. It is noted that all the average film thicknesses reported in this study are calculated as the mean lubricant film thickness within a circular contact region centered at the origin of the computational domain, with a radius equal to the Hertzian contact half-width. Such measurement is the representative of the overall performance of the lubricant film rather than those of the local features or two extreme cases, i.e., the minimum film thickness, $h_{\min}$, which represents the minimum distance from the rough peak to the oil film surface, and the maximum oil film thickness, $h_{\max}$, which represents the maximum distance from the rough valley to the film surface. This selection is based on a comprehensive consideration of multiple film thickness parameters. Although the solver can obtain film thickness values

at any point (such as the central film thickness h_c or the minimum film thickness $h_{\min}$), the average film thickness provides a more stable characterization of the overall lubrication behavior. The central film thickness h_c is susceptible to significant influence from local geometric features of the texture, introducing random biases. The minimum film thickness $h_{\min}$ often becomes ineffective due to asperity contact under mixed lubrication conditions, losing its comparative significance. In contrast, the average film thickness, as a regional integral quantity, reflects the overall distribution characteristics of the lubricant film.

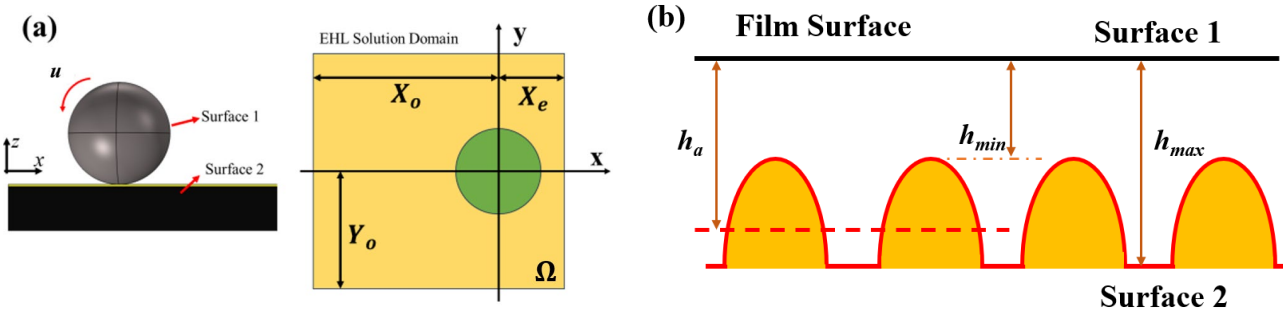


Figure 2. Schema of EHL model description. (**a**) Schematic diagram of point contact EHL solution domain, (**b**) diagram of surface film thickness. In (**a**), the yellow square denotes the EHL solution domain, while the green circle represents the Hertzian contact circle, where X_o, X_e are the distance from the boundaries of the computational domain to the Y-axis ($X_o = 1.9$, $X_e = 1.1$). Y_o is the distance from the top or bottom boundary of the computational domain to the X-axis ($Y_o = 1.5$). In (**b**), h_{min} and h_{max} indicate the local minimum and maximum film thicknesses, and h_a represents the average film thickness.

It was assumed that the viscosity of the lubrication oil is pressure-dependent, and commonly used viscosity equations were provided by Barus' Law. The density of the lubrication oil was also a function of pressure as defined by Dowson–Higginson. The lubrication fluid is governed by the Reynolds equation. For the numerical solution of the Reynolds equation, a multigrid method was employed. The equation was discretized using central and forward differential methods, and then solved interactively. The film thickness was composed of initial film thickness, the macro-contact geometry from the ball, the elastic deformation of the surfaces, and micro-roughness of surfaces 1 and 2. The surface elastic deformation under the action of normal pressure was calculated by using Boussinesq integration. The elastic deformation of rough surfaces was numerically analyzed by the discrete-convolution and FFT (DC-FFT) algorithm presented by Liu et al. [30]. The total load was balanced by two components, i.e., the fluid dynamic pressure supported by the lubrication oil film and contact pressure between the rough solid surfaces. The analysis was directed at the steady-state scenario solved by iteration. The reported average film thickness are spatial periodic averages, which under periodic steady-state conditions are equivalent to temporal averages in the laboratory coordinate system. The computational grid within the domain consisted of 256×256 uniformly spaced nodes, corresponding to a grid size of $\Delta X = \Delta Y = 0.0117$. Under the basic operating conditions as listed in Table 1, the Hertzian contact radius for smooth surfaces was 206 μm. Therefore, for bumps surfaces, the contact area can cover approximately several to several hundred bumps depending on their design parameters. For grooved surfaces, the contact area can cover 4 to 16 grooves, and the number depends on the spacing between the textures.

Table 1. Basic working conditions and analytical results for the EHL simulations.

Parameter	Value
Velocity u/(m/s)	0.1
Radius of the ball r_{ball}/(mm)	12.9
Load W/(N)	100
Young's modulus of the ball E_1/(GPa)	200
Young's modulus of the flat material E_2/(GPa)	200
Poisson's ratio of the ball v_1	0.3
Poisson's ratio of the flat material v_2	0.3
Lubrication oil viscosity η/(Pa·s)	0.096
Pressure viscosity coefficient α/(Pa^{-1})	18.2×10^{-9}
Lubricant density ρ/(g/cm^3)	0.8
Hertzian contact radius r_a/(μm)	206
Hertzian contact pressure p_H/(Mpa)	1120
Hamrock–Dowson analytical central film thickness h_c/(nm)	101.83
Hamrock–Dowson analytical minimum film thickness $h_{\min}$/(nm)	58.91

Film thickness is commonly regarded as a key indicator of lubrication performance. However, in the field of mixed lubrication, the load is jointly supported by the lubricant film and the asperity contacts. Therefore, the film thickness is not solely attributed to hydrodynamic pressure but may also result from the solid contacts provided by surface asperities. To more comprehensively assess the performance in mixed lubrication region, contact load ratio (denoted as β_c) is also reported as an evaluation metric. This ratio quantifies the proportion of the total load carried by asperity contacts and is calculated as follows:

$$\beta_c = \frac{\iint P_{h=0} d\Omega}{W} \tag{3}$$

where W represents the applied load under operational conditions, and $P_{h=0}$ refers to the solid-to-solid contact pressure in regions where the film thickness is zero, i.e., the contact pressure within the contact area. Ω represents the entire computational domain for the EHL analysis.

3. Results

Three types of surface patterns were carefully designed and numerically generated as described in the Methods Section to study the influences of texture type, orientation, and their key geometric parameters on the lubrication. The designed surface patterns began with the isotropic and anisotropic bump array surfaces, then transitioned to groove patterns by reducing the center distance along either one axis, and finally evolved into herringbone-structured surfaces by introducing another wave number k_j. The EHL study focused on the motion state of a ball and its counterpart in pure rolling, where both surfaces moved at the same speed. The working condition parameters used are listed in Table 1 except for the analysis in Section 4.2 where different velocities were involved. Under the listed working condition in Table 1, each surface simulation case satisfies the load balance condition. According to Hamrock–Dowson equations, the central film thickness at the contact center of the smooth surface is 101.83 nm, and the minimum film thickness is 58.91 nm.

3.1. EHL Results of Smooth Surfaces

Prior to the analyses of textured surfaces, the lubricating state of the smooth surface under basic working conditions is given for reference. As shown in Figure 3, because the smooth surface contains no asperities and the hydrodynamic film generated by the

entrainment effect is sufficient to fully sustain the load under the basic working conditions, a full-film EHL state is observed within the studied conditions. Here, the average film thickness h_a = 85.97 nm. The asperity load ratio $\beta_c = 0\%$, indicating that the entire load is supported by the lubricant film, and no solid contact occurs between the surfaces.

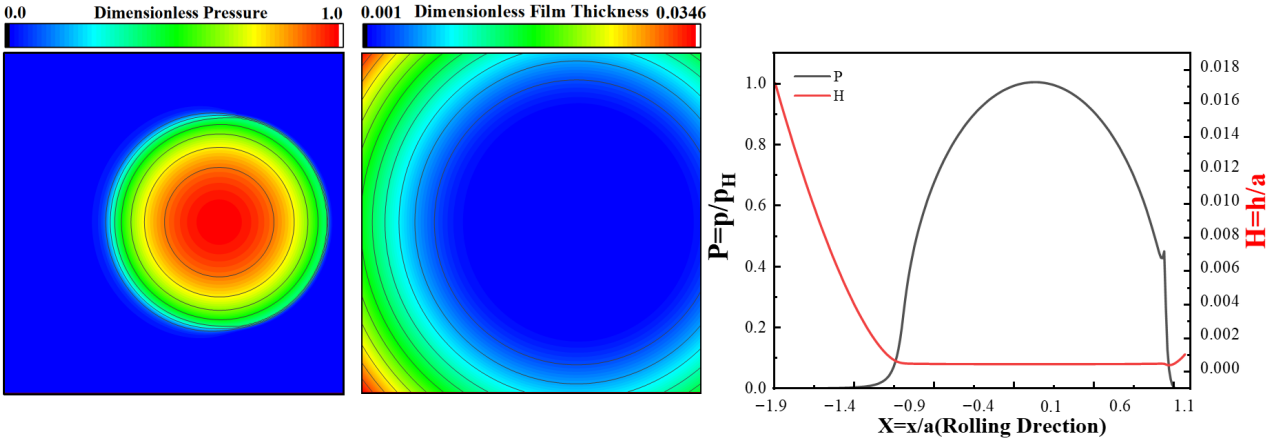


Figure 3. The film thickness and fluid pressure of the smooth surface.

3.2. EHL Results of the Bump Array Surfaces

(1) Isotropic bump array surfaces

As depicted in Figure 4, the structural parameters of that define the isotropic bump array surface are d (specifically $d = d_x = d_y$ for isotropic bump array), A, and r, respectively. Their effects on lubrication performances were studied by varying one and fixing the rest.

As shown in Figure 4a, when the spacing between bumps increases, film thickness h_a are about 75 to 115 nm, while the contact load ratio β_c changes from 0% to 20%. The values seem irregular, but the trends of two curves are largely opposite. This is consistent with the common understanding of film thickness and asperity load ratio relationship, which stated that the greater the film thickness, the lower the probability of asperity contact. The irregularity in the film thickness variation may be due to partial bumps which may exist at the boundary of the Hertzian contact radius, which is the core region for calculating the oil film thickness. As shown in Figure 4b, increasing bump height A leads to a gradual rise in both h_a and β_c. When height A is 0.1 μm, β_c is 0%, and the lubrication mode of the surface at this time is full-film lubrication. As the height of the bumps increases by a few hundred microns, which are way too large as compared with the film thickness, the bump peaks break the lubricating oil film. β_c gradually increases, indicating worse oil supporting. However, the tall bump brings in significant oil storage capacity, which led to an enlarged averaged film thickness with a high contact load ratio. The same trend of h_a and β_c is a sign of poor hydrodynamic lift. Although average film thickness increases, solid-to-solid contacts increases, which may be detrimental to the mechanical parts. The results from different root radii of the bumps are shown in Figure 4c, as the root radius r increases from 6 μm to 19 μm, the surface topography deviates from smooth surfaces, leading to increases in both film thickness h_a and the contact load ratio β_c. However, when r reaches 25 μm, the larger bumps fill the gaps, causing the surface topography to gradually approach smoothness, thereby reducing the load-bearing ratio. The two curves exhibit similar trends, indicating that hydrodynamic lift is not the dominant factor.

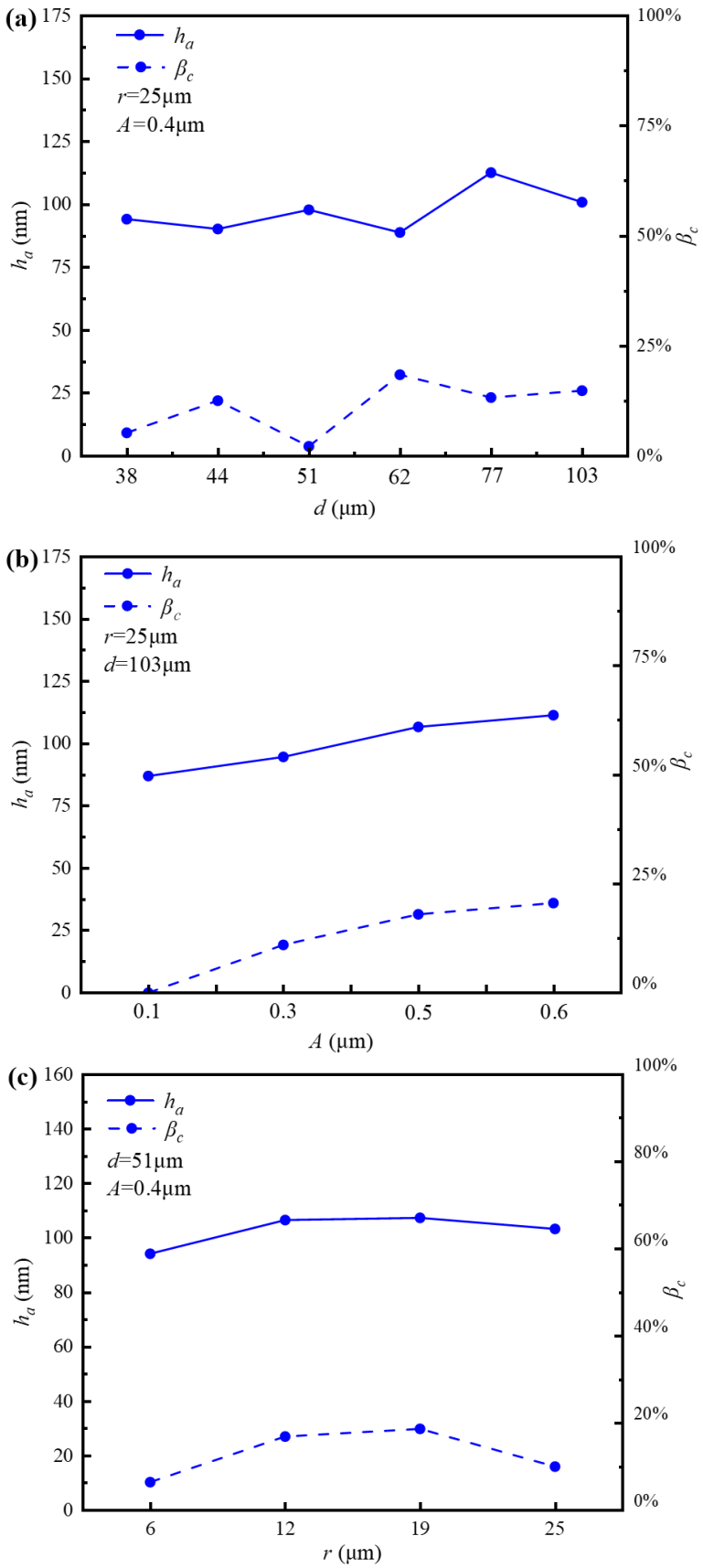
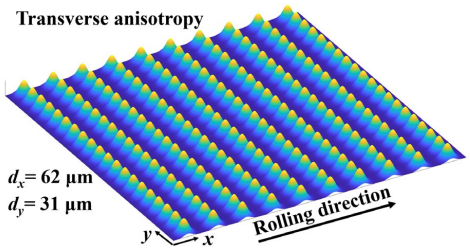
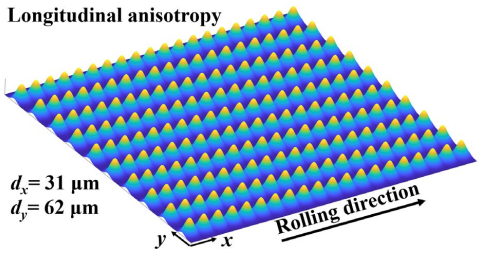


Figure 4. Influence of three geometric parameters, (**a**) spacing d ($d = d_x = d_y$), (**b**) height A, (**c**) root radius r, of isotropic bump array surfaces on their lubrication performance.

(2) Anisotropic bump array surfaces

The center distances of two adjacent bumps in the x and y directions, d_x and d_y, may be set to distinct values to create anisotropic bump array surfaces, whose orientation with respect to the rolling direction will influence the lubrication performances. Since the rolling direction is fixed as along x-axis in this study, we numerically generated two surface groups for comparative analysis by systematically varying either one of the texture spacing d_x or d_y while maintaining constant texture radius r and height A, as specified in Table 2.

Table 2. Design parameters for two groups of anisotropic bump array surfaces.

Parameters	Transverse Configuration	Longitudinal Configuration
r	12 μm	12 μm
A	0.5 μm	0.5 μm
d_x	Fixed, selected from 51 μm, 62 μm, and 77 μm	Variable, ranged from 12 μm to 77 μm
d_y	Variable, ranged from12 μm to 77 μm	Fixed, selected from 51 μm, 62 μm, and 77 μm
Example		

For the longitudinal configuration, three sets of surfaces were studied with d_y fixed to be 51 μm, 62 μm, and 77 μm, respectively, while d_x varies from 12 μm to 77 μm. The bump root diameter, r, is set to 21 μm, the bump height, A, is chosen as 0.5 μm. The average film thickness and contact load ratio of anisotropic bump array surfaces in longitudinal configuration are plotted in Figure 5. The average film thickness, h_a, doesn't change much with respect to d_x, while the contact load ratio β_c apparently increases as d_x reduces, indicating that the oil film load-bearing capacity of the longitudinal configuration of bump array surface is relatively poor as compared with those of transverse configuration. When the bump spacing is large ($d_x > 37$ μm), fluctuations in film thickness occur due to smaller number of bumps under contact. In addition, when the spacing in the y-direction is smaller (triangle symbol vs. square symbol), the film thickness shows no significant change, but the contact load ratio increases significantly. Such performance indicates that under longitudinal configuration of the bump array, dense textures studied structures are unfavorable for lubrication application as the load bearing from the fluid is getting worse although the averaged film thickness remains unchanged.

For the transverse configuration, three sets of surfaces were studied with d_x fixed to be 51 μm, 62 μm, and 77 μm, respectively, while d_y varies from 12 μm to 77 μm. The bump root diameter, r, is set to 21 μm, and the bump height, A, is chosen as 0.5 μm. The average film thickness and contact load ratio of anisotropic bump array surfaces in transverse configuration are plotted in Figure 6. The average film thickness shows significant decreases when d_y increases. The contact load ratio shows a minor drop when d_y increases. When d_y is large, the bumps are sparsely distributed and more close to isotropic bump array surfaces. As d_y approaches to 12 μm, the number of bumps in the y-direction increases, thereby enhancing hydrodynamic effect. In addition, the average film thickness of surfaces with d_x = 77 μm is close to those with d_x = 51 μm, and both are overall greater than the average film thickness of surfaces when d_x = 62 μm. Therefore, the

variation in the number of transverse textures and the lubricating film thickness exhibits a nonlinear relationship.

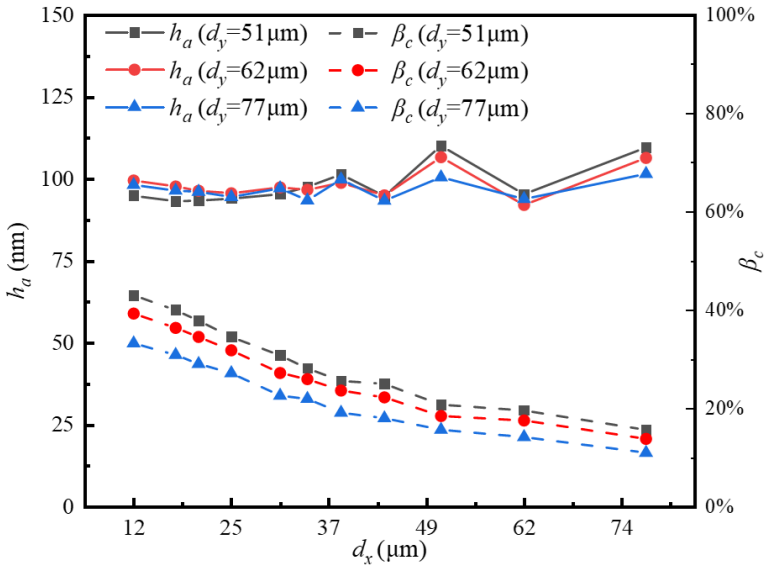


Figure 5. The average film thickness and contact load ratio of anisotropic bump array surfaces in longitudinal configuration.

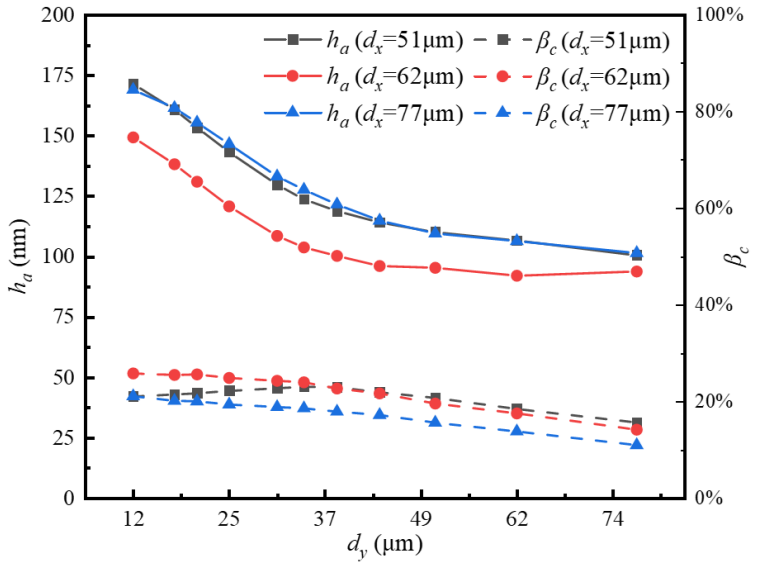


Figure 6. The average film thickness and contact load ratio of anisotropic bump array surfaces in transverse configuration.

As observed from the right ends of the curves in Figures 5 and 6, it can be seen that although the average film thickness of bump array surfaces with more isotropic bumps is not large, the contact load ratio β_c is much smaller as compared with that of anisotropic bumps surfaces (on the left end of curves in Figures 5 and 6). This indicates that more isotropic bump array surfaces can form a high-load-bearing hydrodynamic oil film. Compared with in transverse rough surfaces group, a significant increase in h_a does not reduce the β_c value, which suggests that the oil film load-bearing capacity of anisotropic transverse grooved surfaces is inferior to that of isotropic bump array surfaces. For the longitudinal rough surfaces group, when transitioning from isotropic bump array surfaces to anisotropic longitudinally surfaces, h_a shows no significant change, but β_c increases significantly, which might because the oil leakage along the rolling direction reduces the oil film's load-bearing capacity.

In summary, the lubrication performance of isotropic bump array surfaces is superior to that of anisotropic surfaces. When anisotropy is present, transverse grooved surfaces perform significantly better than longitudinal surfaces.

3.3. EHL Results of the Groove Surfaces

The longitudinal or transverse groove surfaces are firstly studied using a cosine wave, with the number and height of the ridges adjusted by changing the wave number, k_g, and the amplitude, A, of the cosine function. Specifically, the larger the value of k_g, the denser the grooves within the simulation domain.

The influences of wave number, k_g, on the average film thickness and contact load ratio for longitudinal groove surfaces (blue dots) and transverse groove surfaces (black squares) are plotted in Figure 7a. For longitudinal groove surfaces, the averaged film thickness barely changes, which is consistent with the experimental observations with longitudinal rough surfaces by Guegan et al. [1]. However, the contact load ratio shows significant differences, which changed from 0% to 80%. As the wave number, k_g, increases from 4 to 9, the grooves get thinner, and a larger deformation results in a significant rise in the contact load ratio of the longitudinal rough surfaces. For transverse groove surfaces, the trends of average film thickness and contact load ratio are opposite, which aligns with the understanding of relationship between film thickness and asperity load, indicating that the formation of the oil film on transverse grooves is primarily driven by hydrodynamic effects.

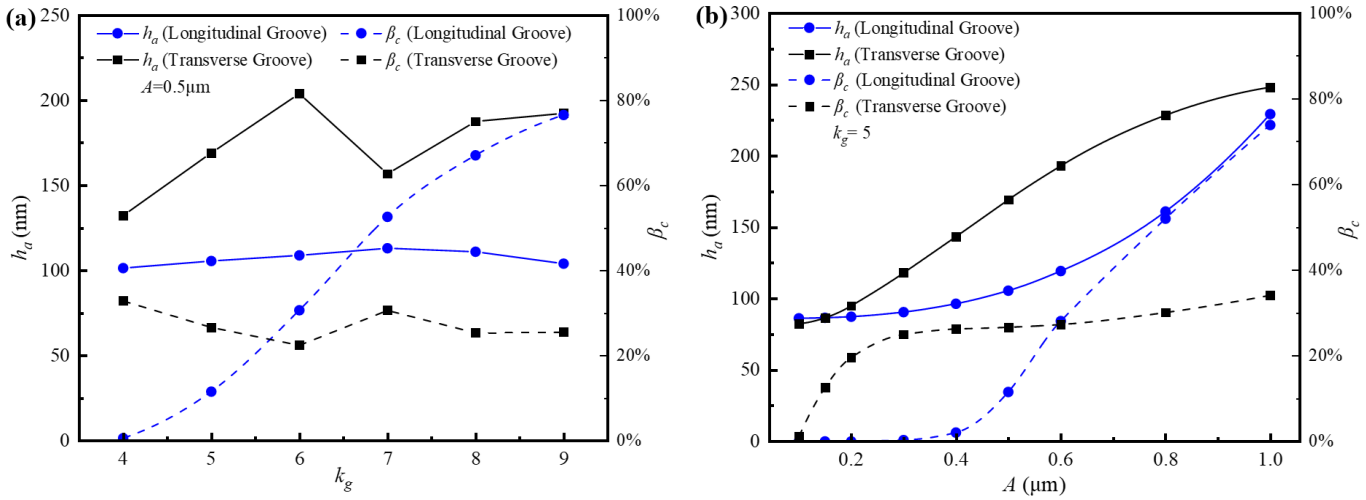


Figure 7. Influence of cosine groove surfaces structural parameters, (**a**) wave number k_g , (**b**) amplitude A, on lubrication performance.

The influences of amplitude, A, on the average film thickness and contact load ratio for longitudinal groove surfaces (blue dots) and transverse groove surfaces (black squares) are plotted in Figure 7b. As the amplitude of the surface grooves increases, the variation trends of h_a and β_c are consistent for both transverse and longitudinal groove surfaces. Specifically, for the longitudinal groove surface, h_a and β_c first increase slowly and then increase rapidly, while for the transverse groove surface, h_a and β_c first increase rapidly and then increase slowly. The film thickness increase is due to the increased oil storage capacity with larger amplitude for the longitudinal grooves, while transverse groove surfaces is a combination of micro-EHL effect and oil storage capacity.

Nonetheless, as the wave number of the cosine function increases, the ridge spacing and ridge width change simultaneously, making the influences of those two structural parameters on lubrication difficult to investigate. As observed from the anisotropic bump array, groove surfaces can be created by superimposing bumps along the x or y axis. This

method allows for independent control of surface geometric parameters, such as ridge height A, ridge spacing d, and ridge half width r, and their influences on the EHL results of such groove surfaces along longitudinal and transverse configurations are shown in Figures 8 and 9, respectively.

The inferences of various ridge spacing d on the average film thickness and contact load ratio of longitudinal groove surfaces (r = 12 μm and A = 0.5 μm) is shown in Figure 8a. As the ridge spacing d increases from 39 μm to 103 μm, the number of grooves decreases gradually, the film thickness h_a first increases and then decreases, while contact load ratio β_c remains stable when d is small and then decreases gradually. When the groove spacing d increases from 39 μm to 62 μm, where the ridge contact provides significant load support, and the space available for lubricant storage gradually enlarges. When d exceeds 62 μm, the gradual reduction in film thickness is mainly due to the decreased number of ridges on the surface, which reduces the contact area ratio and contact load ratio.

As shown in Figure 8b, with ridge spacing d fixed at 77 μm and ridge height A fixed at 0.5 μm, the ridge half width r increases from 6 μm to 31 μm. Both h_a and β_c show an overall decreasing trend. This is because as the ridge width increases, the ridge shape changes from sharp ridges to gentle undulations. In the former case, the lubricant film formation involves load sharing by asperities, whereas in the latter case, the surface tends toward smoothness, resulting in β_c dropping to 0% when r equals and larger than 19 μm.

With the ridge half width r fixed at 12 μm, the effect of ridge height A on lubrication was studied for two ridge spacings, d = 44 μm and d = 77 μm. As shown in Figure 8c, as the ridge height increases from 0.1 μm to 1 μm, both h_a and β_c increase. When the ridge height is 0.1 μm, full-film lubrication occurs (β_c = 0%). As the ridge height increases, the grooves break the hydrodynamic film, causing β_c to gradually increase. When ridge height is 1 μm, the asperity load ratio β_c approaches 100%. At this stage, the lubricant film merely fills the gaps supported by the asperities and almost does not participate in load bearing. In addition, when the ridge spacing is larger (d = 77 μm), h_a grows more rapidly for shallow grooves, because a larger ridge spacing increases the surface's oil storage capacity. The influence is more obvious when ridge height is small.

The influences of various ridge spacing d on the average film thickness and contact load ratio of transverse groove surfaces (r = 12 μm and A = 0.5 μm) is shown in Figure 9a. The average film thickness slightly increases with the transverse ridge spacing d from 39 μm to 103 μm, with little oscillations. The contact load ratio, β_c, exhibits an opposite trend to average film thickness. This is an indication that the increases in film thickness caused by changing d originates from enhancement of the hydrodynamic pressure from the lubricant film. The irregular variation of h_a with changes in transverse groove spacing d is due to the irregular contact position with respect to the ridge center.

As shown in Figure 9b, as the ridge width increases, the film thickness h_a and the contact load ratio β_c first increase and then decrease. An increase in the ridge half width r reduces the surface's oil storage capacity. The consistency in the trends of h_a and β_c indicates that the variation in film thickness caused by changing the transverse ridge half width r originates from changes in asperity load carrying.

With ridge half width r fixed at 12 μm, the influences of ridge height on lubrication was studied for two ridge spacings, d = 44 μm and d = 77 μm. As shown in Figure 9c, as the ridge height increases from 0.1 μm to 1 μm, both h_a and β_c increase. When the ridge height is 0.1 μm, full-film lubrication occurs (β_c = 0%). When ridge height A is large, contact load ratio β_c is relatively smaller as compared with those from the longitudinal cases (for longitudinal groove surfaces, when A is 1 μm, β_c approaches 100%). This indicates that the hydrodynamic effect of transverse grooves is superior to that of longitudinal grooves, and

under mixed lubrication conditions, transverse groove surfaces are more likely to form an effective lubricant film to support the loading.

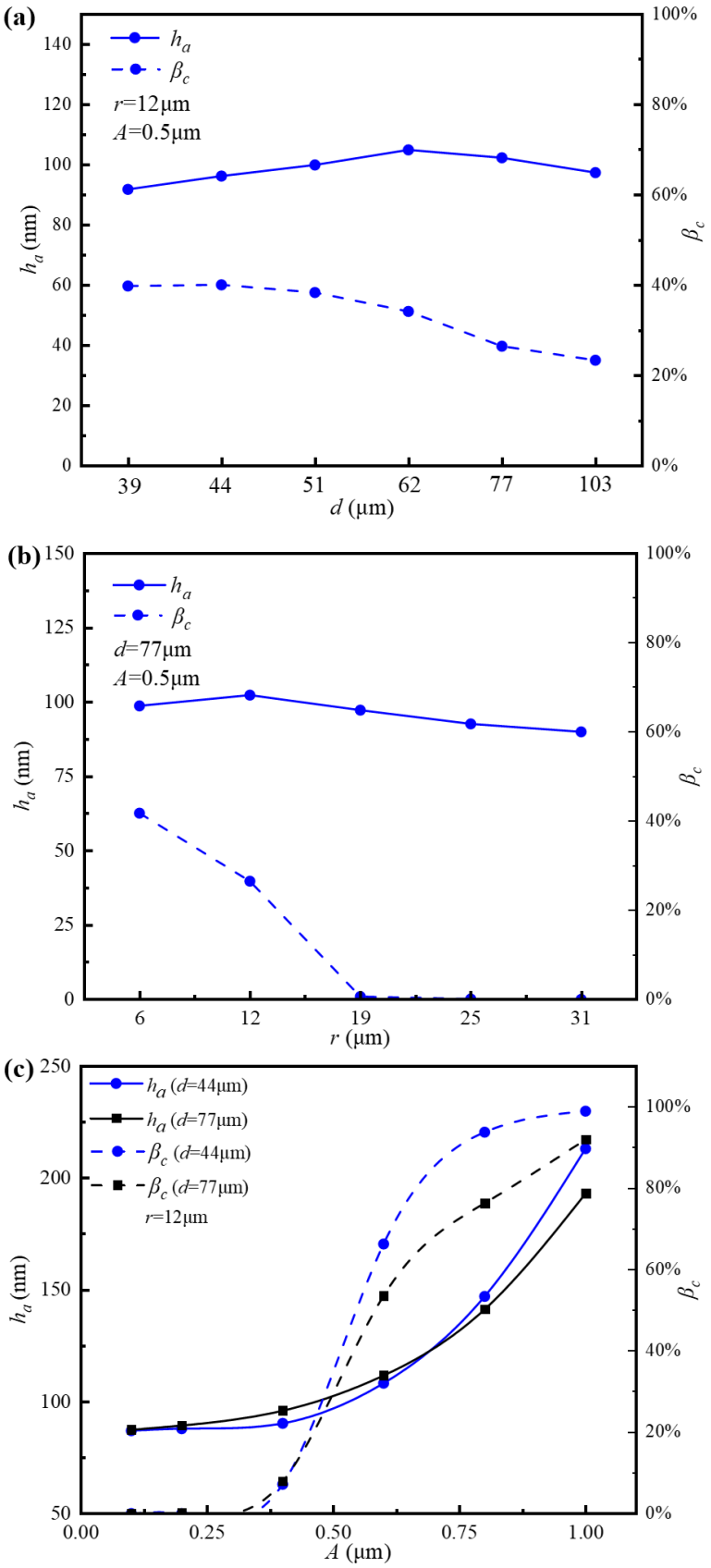


Figure 8. Influence of geometric parameters (**a**) spacing d, (**b**) half width r, (**c**) height A on the lubrication performance of longitudinal groove surfaces.

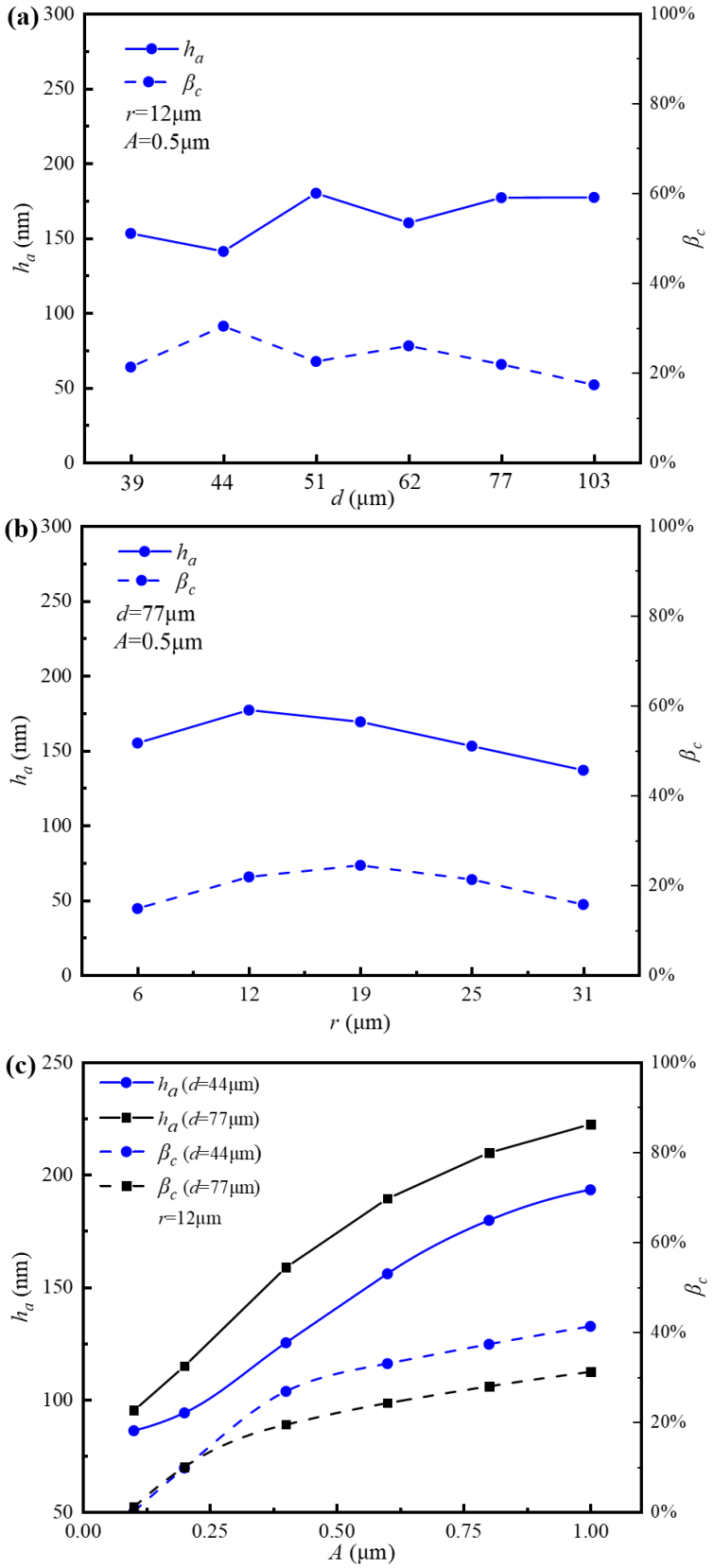


Figure 9. Influence of geometric parameters (**a**) spacing d, (**b**) half width r, (**c**) height A on the lubrication performance of transverse groove surfaces.

The dominating film formation mechanisms of transverse and longitudinal groove surfaces differ. For transverse groove surfaces, when ridge spacing d is varied, the trends of film thickness h_a and contact load ratio β_c are opposite, indicating that the micro-EHL effect is significant. In contrast, for longitudinal groove surfaces, when groove spacing d is changed, the trends of h_a and β_c are complex, suggesting that the hydrodynamic lift is marginal due to easier oil flow along grooves. This is especially true when the ridge height is large, where β_c approaches 100% as ridge height close to 1 μm.

The hydrodynamic effect generated by transverse groove surfaces is superior to that of longitudinal groove surfaces. With surface ridge spacing d fixed at 44 μm and ridge height fixed at 1 μm, the film thickness contour plots for transverse and longitudinal groove surfaces are shown in Figure 10. Along the rolling direction, the transverse groove surface forms a thick hydrodynamic lubricant film next to the ridges, as shown by the oval stripes enclosed by contour lines of dimensionless film thickness of 0.0025 (dimensional film thickness is 515 nm) in Figure 10b. Along the vertical direction passing through the origin of the texture, it can be observed that the film thickness in the central region of the transverse groove surface is significantly higher than that of the longitudinal groove surface. This observation is consistent with the oil film observed experimentally by Guangteng et al. [14] and Kaneta et al. [31], which states there is a thick oil film region immediately adjacent to the asperity ridge on the contact exist side. In contrast, the longitudinal groove surface experiences lubricant leakage along the flow direction, resulting in smaller film thickness between grooves, as shown in Figure 10a.

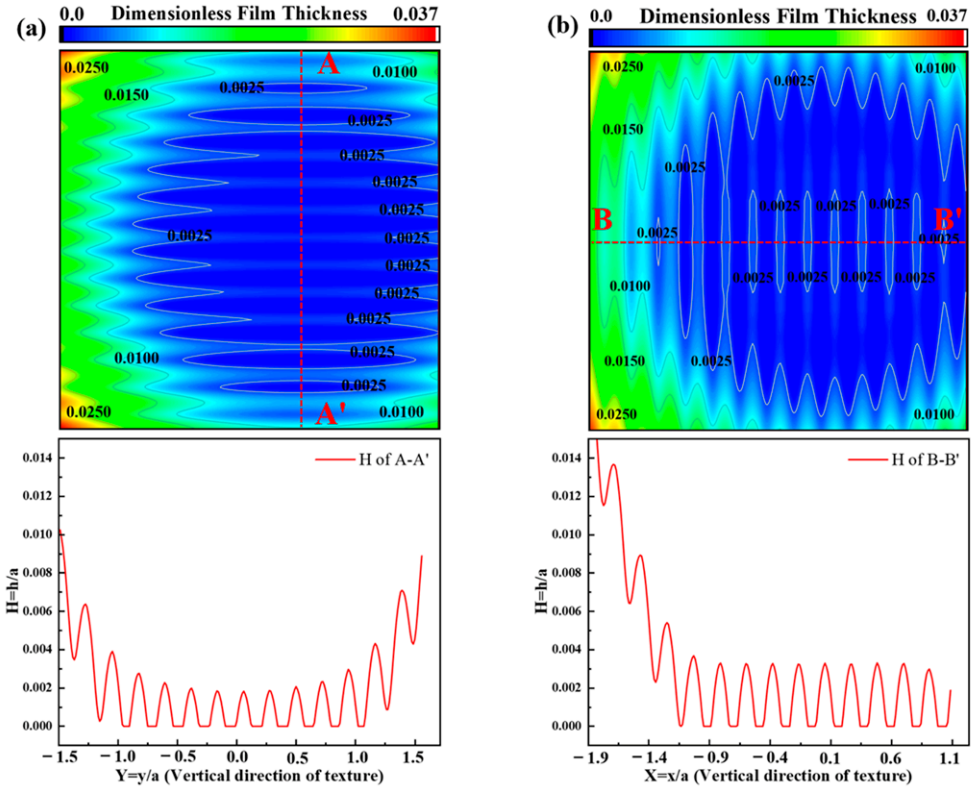


Figure 10. Dimensionless film thickness contour plot and cross-sectional film thickness of the surface with fixed groove spacing d = 44 μm and groove height A = 0.5 μm. (**a**) Longitudinal groove surface, (**b**) transverse groove surface.

3.4. EHL Results of the Herringbone Surfaces

In the numerical simulation of the herringbone surface, two parameters, namely the long wavelength $2\pi/k_j$ and the short wavelength $2\pi/k_g$, are controlled to generate surfaces with distinct features. k_g governs the number of ridges within the simulation domain, while k_j determines the extent of surface undulations of each ridge, with large k_j corresponding to intense surface wrinkling. Figure 11 illustrates the transverse herringbone surfaces with different k_j values (k_g = 5).

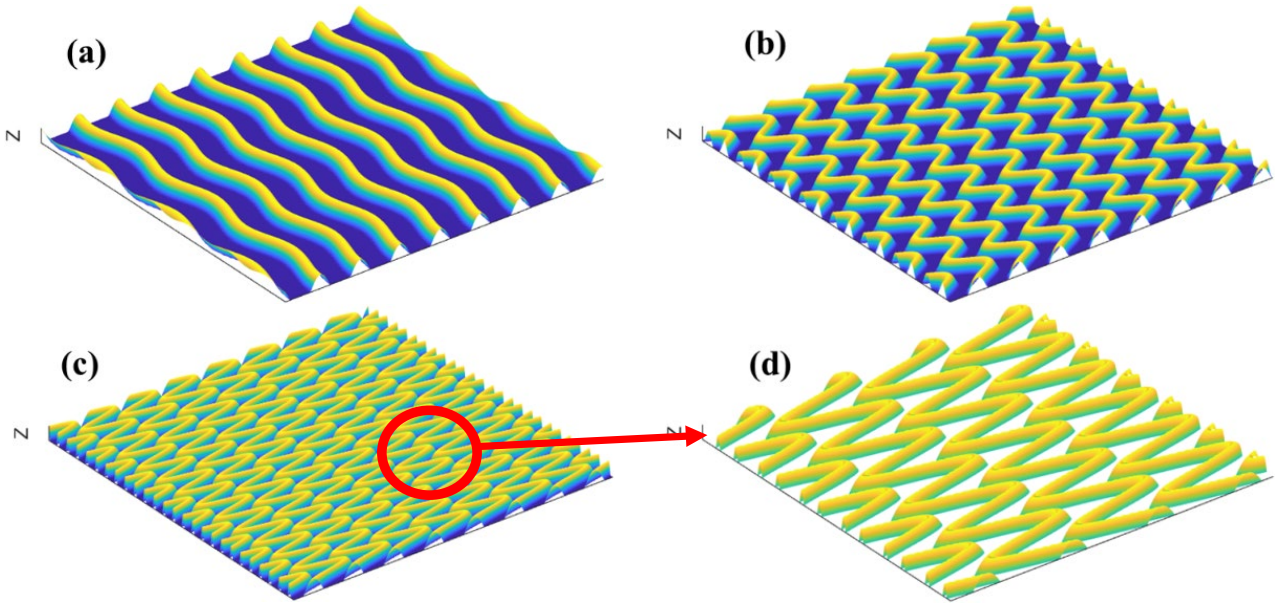


Figure 11. Impact of long wavelength $2\pi/k_j$ on the wrinkling of herringbone surface. (**a**) $k_g = 5$, $k_j = 2$; (**b**) $k_g = 5, k_j = 5$; (**c**) $k_g = 5, k_j = 8$; (**d**) zoomed-in view of (**c**).

The influences of different wave numbers of the transverse herringbone surface on average film thickness and contact load ratio are shown in Figure 12. When k_g is smaller than 6, the lubrication results are not representative as the number of topological features on the surface is too small. Long wave number k_g of 6, 8, and 10 are chosen for this part of study. As observed in Figure 12, changing the wave number k_g does not significantly alter the average film thickness, h_a, indicating that for transverse herringbone surfaces, varying the number of ridges on the surface has little effect on h_a. As the wave number k_j increases, the wrinkling of the herringbone surface becomes more pronounced. When k_j is small ($k_j \leq 5$), the film thickness h_a remains at a relatively high level ($h_a > 160$ nm). However, when k_j is large ($k_j > 5$), h_a drops dramatically. This is because, when k_j is small, the transverse herringbone surface behaves similarly to the transverse grooved surface, forming a localized hydrodynamic film behind the grooves in the rolling direction, while the contact load ratio β_c remains low. As k_j approaches 5, the wrinkles of the herringbone surface become inclined at approximately 45°, and the transverse herringbone grooves gradually transform toward a longitudinal orientation. Consequently, the hydrodynamic effect weakens, asperity contact intensifies, and β_c gradually increases.

Similar to transverse herringbone surfaces, longitudinal herringbone surfaces exhibit comparable characteristics, as shown in Figure 13. For longitudinal herringbone surfaces, the wave number k_g has a significant impact on the film thickness h_a. The larger the k_g, the smaller the h_a and the larger the contact load ratio β_c. As the wave number k_j increases from 1 to 9, the wrinkling of the longitudinal herringbone surface intensifies. When $k_j < 7$, h_a gradually increases and β_c gradually decreases. This is because increasing the wrinkle density can reduce longitudinal leakage and, to some extent, enhance the

hydrodynamic effect induced by transverse anisotropic textures, thereby forming a more stable hydrodynamic oil film. However, when $k_j \geq 7$, h_a gradually decreases and β_c increases. This is because excessive wrinkling may reduce the oil storage capacity.

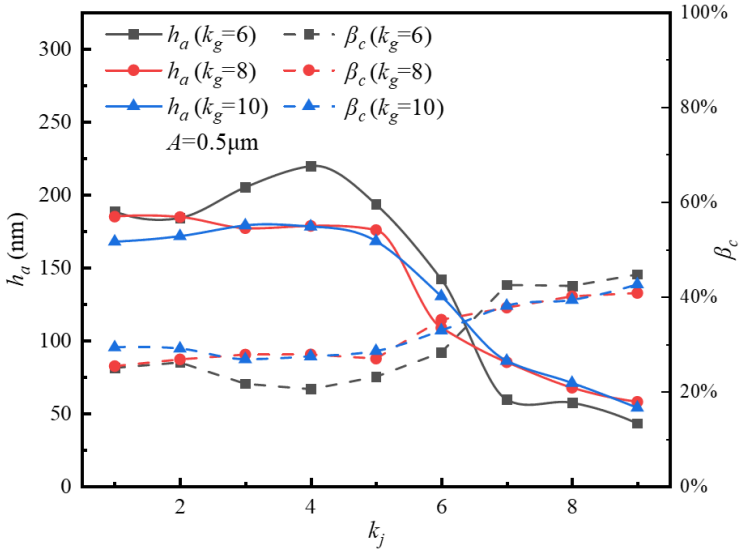


Figure 12. Influences of wave numbers on the average film thickness and contact load ratio of transverse herringbone surfaces.

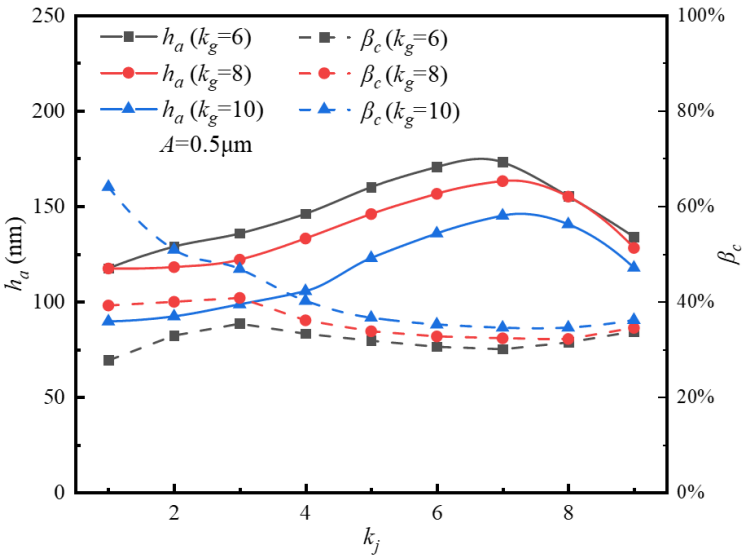


Figure 13. Influences of wave numbers on the average film thickness and contact load ratio of longitudinal herringbone surfaces.

Figure 14 presents the contour plots of the oil pressure distribution (first column), contour plots of oil film thickness (second column), and oil film thickness and pressure profiles across the center line along the rolling direction (third column) of the longitudinal herringbone surfaces (when $k_g = 8$ and k_j = 0, 4, 8, respectively). As shown in Figure 14a, when $k_j = 0$, the herringbone surface degenerates into a groove surface, and a secondary pressure peak emerges near the edge of the Hertzian contact ellipse (black line). Since the ball is located on the top surface of the ridge in the center, the two mating surfaces at this spot are in full contact, and the film thickness (red line) is nearly zero. As k_j increases from 0 to 4, the herringbone surface's wrinkles transition transversely, mitigating the oil film leakage caused by longitudinal grooves. The pressure concentrated at asperity contacts

shifts to the oil film, and the film thickness contour plot exhibits periodic variations corresponding to the undulations of the herringbone wrinkles. As shown in Figure 14c, when $k_j = 8$, the herringbone wrinkles undergo further transverse transformation, enhancing the hydrodynamic effect, increasing the oil film load-bearing ratio, reducing the contact load ratio, and promoting further shift of pressure concentration from asperity peaks to the oil film, resulting in smoother pressure contour plots.

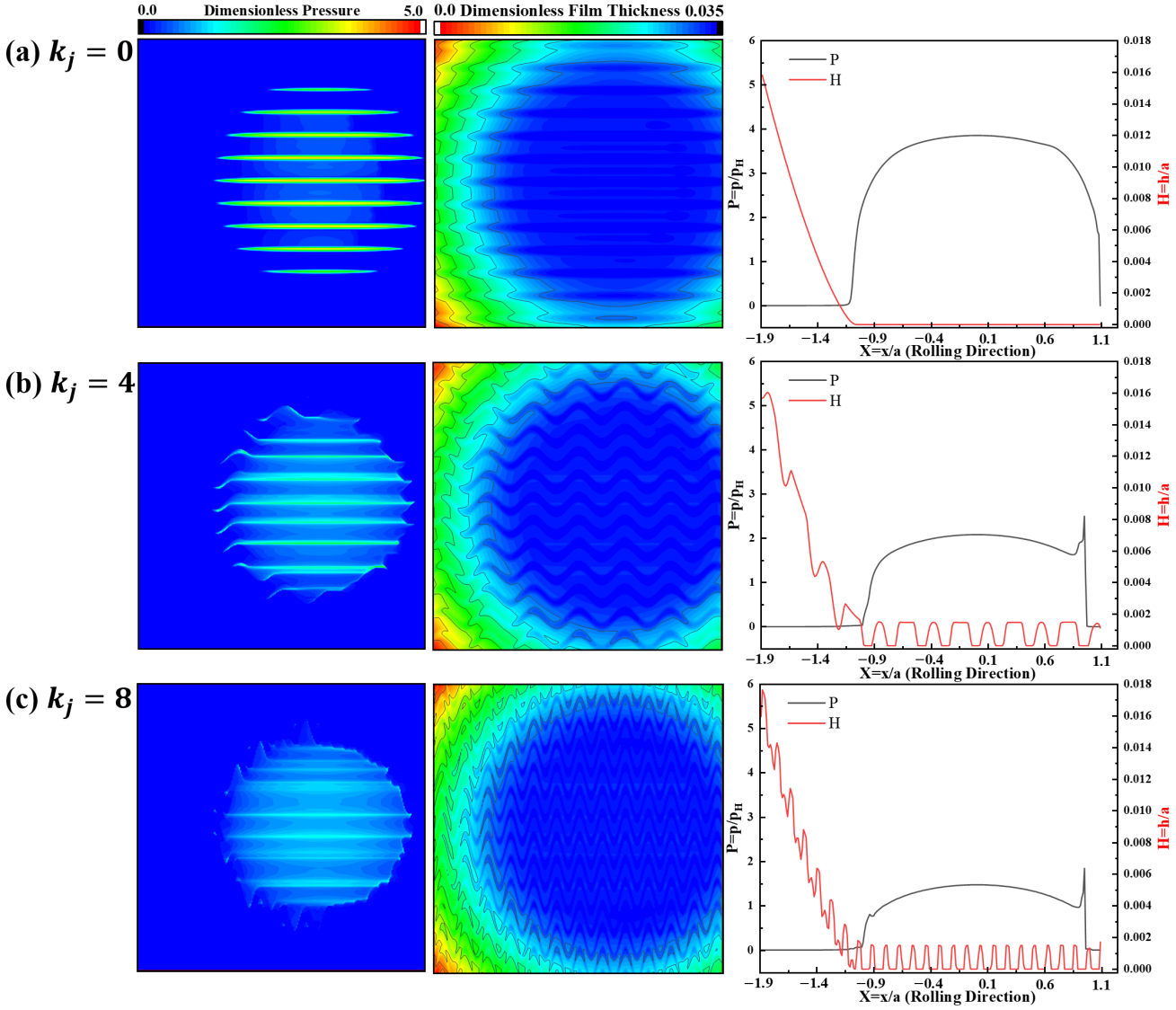


Figure 14. Contour plots of the oil pressure distribution (first column), oil film thickness (second column), and oil film thickness and pressure profiles across the center line along the rolling direction (third column) of the longitudinal herringbone surfaces (k_g = 8 and k_j varies). (**a**) k_j = 0, (**b**) k_j = 4, (**c**) k_j = 8.

Figure 15 presents the contour plots of oil pressure distribution (first column), oil film thickness contour plots (second column), and cross-sectional profiles of oil film thickness and pressure along the centerline in the rolling direction (third column) for the transverse herringbone-textured surfaces (with parameter $k_j = 0$, 4, 8, respectively). As shown in Figure 15a, when $k_j = 0$, the herringbone surface exhibits transverse groove characteristics. Due to sufficient hydrodynamic pressure, the pressure contour plot remains relatively smooth, with noticeable asperity contact pressures only appearing near the edges of the Hertzian contact zone. A relatively thick lubricating film forms along the centerline in the rolling direction. In Figure 15b, when $k_j = 4$, wrinkles develop on the transverse

herringbone surface. Compared to the transverse groove surface, these wrinkles slightly weaken the hydrodynamic pressure effect. The oil film thickness significantly decreases compared to the $k_j = 0$ case, while the pressure contour plot remains relatively smooth, still maintaining a strong hydrodynamic effect. As shown in Figure 15c, when $k_j = 8$, the wrinkles on the transverse herringbone surface shift toward the longitudinal direction, substantially disrupting the hydrodynamic pressure. Leakage occurs along the rolling direction, leading to pressure concentration phenomena in the contour plot and a significant reduction in oil film thickness.

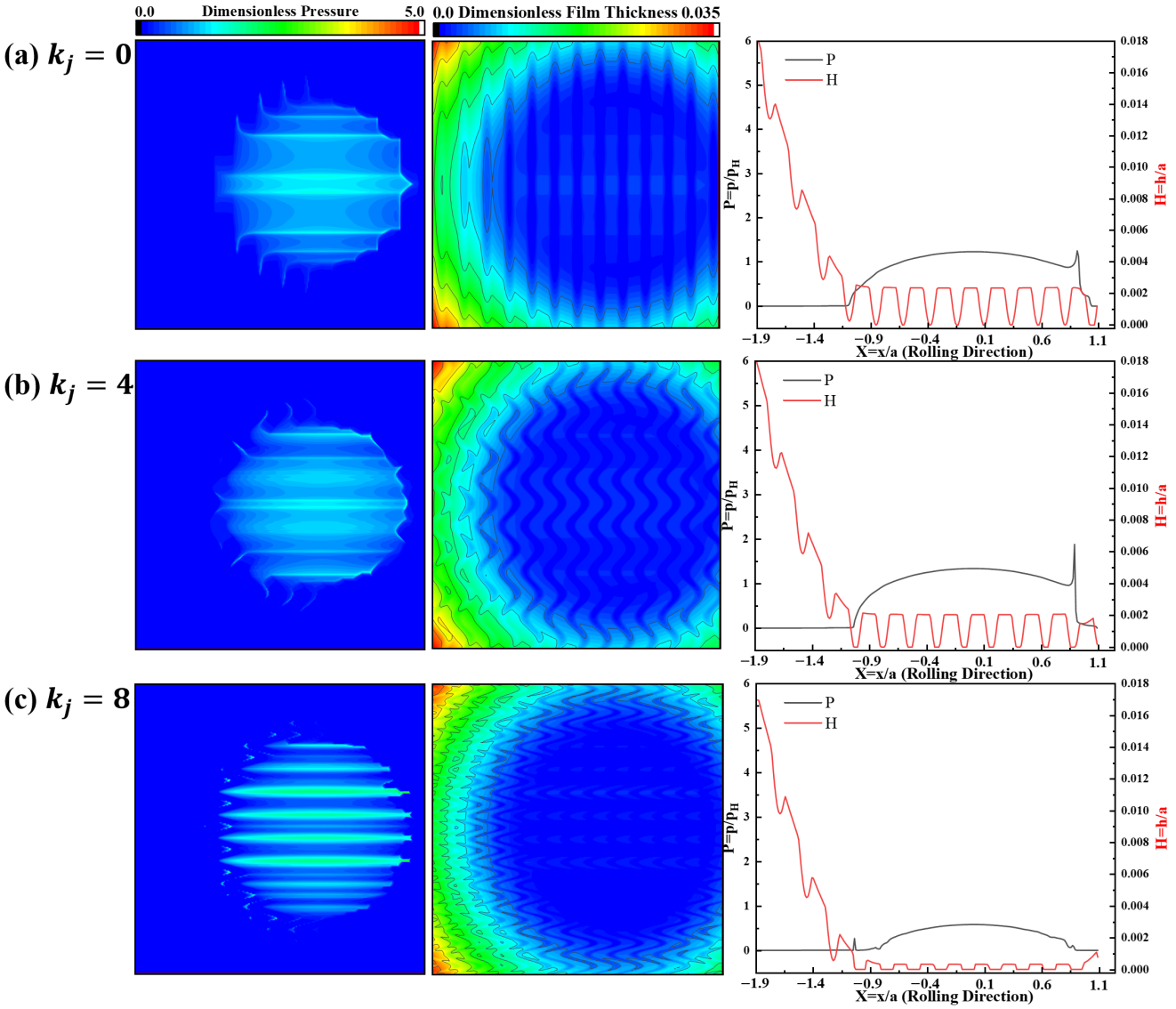


Figure 15. Contour plots of the oil pressure distribution (first column), oil film thickness (second column), and oil film thickness and pressure profiles across the center line along the rolling direction (third column) of the transverse herringbone surfaces (k_g = 8 and k_j varies). (**a**) k_j = 0, (**b**) k_j = 4, (**c**) k_j = 8.

4. Discussions

4.1. Influence of Surface Topology Variations on Film Thickness

Combining the analyses of the three surface types mentioned above, it is evident that increasing the number of bumps along x or y axis on the surface transforms it into a surface with longitudinally or transversely groove surfaces. Reducing the folds in the surface of the herringbone structure will cause it to gradually turn into a groove surface. Therefore,

the fluctuation of film thickness under the same operating conditions for these three types of surfaces are jointly analyzed, as illustrated in Figure 16.

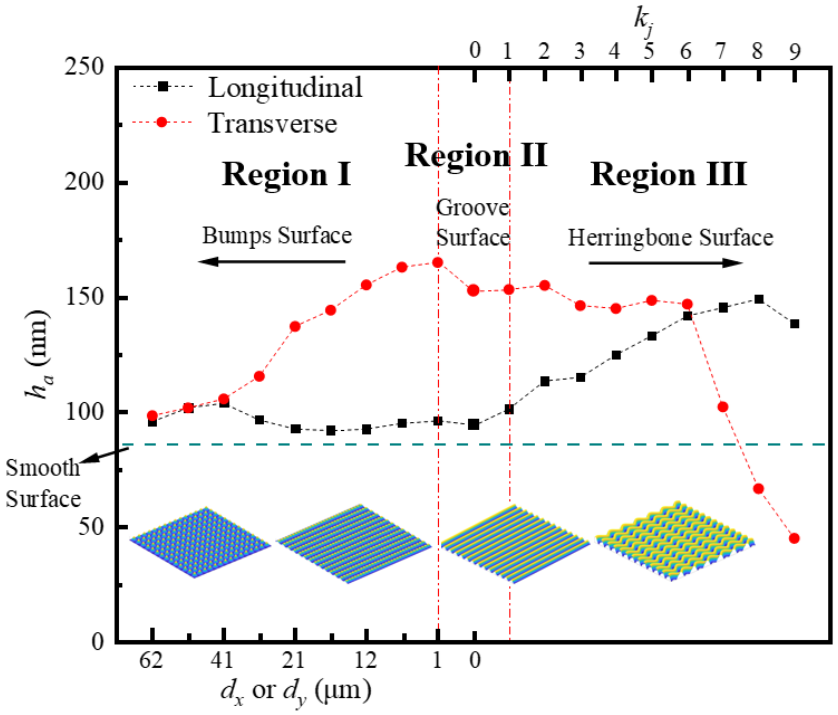


Figure 16. Comparison of film thicknesses of various surfaces along transverse orientation (red dots) and longitudinal orientation (black squares).

The transverse bump array surfaces (red dots in region I) have d_x fixed to be 48 μm, and d_y changes from 1 μm to 62 μm (see horizontal axis on the bottom left of Figure 16). The longitudinal bump array surfaces (black squares in region I) have d_y fixed to be 48 μm, and d_x changes from 1 μm to 62 μm. The ridge distance of groove surfaces and herringbone surfaces are all set as 48 μm. The wave number k_j is chosen from 1 to 9 as shown in horizontal axis on the top right of Figure 16. A larger (Region III) value of k_j indicates a stronger wrinkling of the herringbone structure. The amplitude of all the surface patterns is 0.5 μm, root radius of 21 μm.

For the longitudinal orientation (black squares), the variation in average film thickness is relatively small (similar to Figure 5) during the transition from bump array surfaces to groove surfaces. However, due to the overlap of bumps, the oil storage capacity of the surface is reduced as d decreases. When the longitudinal groove surface transforms into a longitudinal herringbone surface, the film thickness gradually increases. This is because the intensified wrinkling of the longitudinal herringbone surface progressively folded in the transverse direction, thereby enhancing the hydrodynamic lubrication effect and reducing lubricant leakage, as explained in Figure 13.

For the transverse orientation (red dots), as the surface evolves from isotropic bump array surfaces to transversely anisotropic groove textures, the film thickness gradually increases due to the superior hydrodynamic pressure effect generated by the transverse grooves as discussed in Figure 6. When the transverse groove surfaces transform into a transverse herringbone surface, wrinkling appears along the grooves. As the value of k_j increases, the wrinkling becomes more pronounced, progressively impairing the hydrodynamic effect produced by the transverse grooves. The average film thickness gradually decays when k_j is less than 6, and drops drastically when k_j is larger than 6, and even smaller than that of smooth surface. The trend is similar to that in Figure 12.

4.2. The Effect of Sliding Velocity on Lubrication

In view of the significant differences in lubrication performance between transverse and longitudinal textures, an analysis was conducted on groove surfaces with pronounced anisotropy under sliding velocities u ranging from 0.15 m/s to 10 m/s. The groove spacing d is fixed at 44 μm. The average film thickness, h_a, and contact load ratio β_c for transverse and longitudinal ridges with ridge heights of 0.3 μm, 0.5 μm, and 0.8 μm are presented in Figure 17. This study found that as the sliding velocity increases, the average film thickness h_a for transverse and longitudinal groove surfaces both increases. At lower sliding velocities ($u \leq 1$ m/s), the film thickness of transverse groove surfaces is greater than that of longitudinal groove surfaces. At higher sliding velocities ($u > 1$ m/s), the influence of surface anisotropy on film thickness becomes smaller, and at $u = 10$ m/s, the effects of ridge orientation and ridge height on film thickness are minimal. At the same ridge height, A, the contact load ratio, β_c, varies with groove orientation. When the groove height is relatively small (0.3 μm and 0.5 μm) and the sliding velocity is low, the β_c of longitudinal grooves is lower than that of transverse grooves. However, when the ridge height is larger (0.8 μm), the β_c of longitudinal grooves becomes significantly higher than that of transverse grooves. This indicates that under pronounced anisotropic conditions, i.e., when the ridge height is large, the lubrication performance of transverse groove surfaces is superior to that of longitudinal groove surfaces.

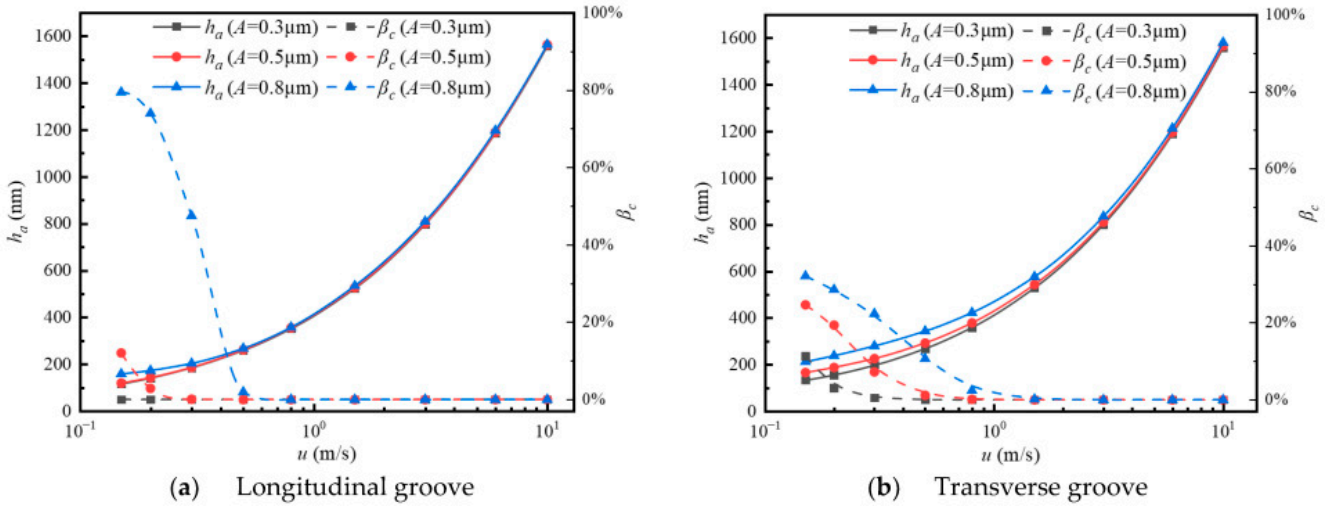


Figure 17. Influence of different sliding speeds on the lubrication performance of grooved surfaces.

The lift-off speeds are reported when the contact load ratio is zero. As observed in three longitudinal groove surfaces, the lift-off speed is 0.8 m/s for the groove surfaces with 0.8 μm amplitude, 0.3 m/s for the groove surfaces with 0.5 μm amplitude, and below 0.15 m/s for the groove surfaces with 0.3 μm amplitude. The value and trend are consistent with experiments [1]. The lift-off speeds of these three surfaces in transverse groove surfaces are 0.3 m/s, 0.8 m/s, and 1.5 m/s for ridge amplitude of 0.3 μm, 0.5 μm, and 0.8 μm, respectively. If no solid-to-solid contact is allowed, longitudinal groove surfaces require a low lift-off speed.

5. Conclusions

This study systematically investigates the influence of surface texture type and orientation on lubrication performance in point-contact mixed elastohydrodynamic lubrication (EHL) by using numerical simulations of bump array surfaces, groove surfaces, and herringbone surfaces. The main findings are as follows:

1. Isotropic bump arrays outperform anisotropic configurations in lubrication efficiency with lower contact load ratios (0–20%), primarily due to effective hydrodynamic pressure generation, which reduces the contact load of asperities.
2. Among textures with pronounced anisotropy, transverse grooves exhibit superior lubrication performance compared with longitudinal grooves, because of strong micro-EHL effects due to enhanced lubricant entrapment behind ridges. The transverse surfaces achieve up to about 50% thicker average films than longitudinal counterparts for the conditions studied.
3. For herringbone surfaces, an increase in the short wavelength k_j intensifies surface wrinkling and alters the direction of surface anisotropy. For instance, as k_j increases, longitudinal herringbone surfaces tend to transition toward transverse orientations, thereby increasing film thickness and reducing surface contact load.

These findings provide practical guidelines for engineering textured surfaces in tribological applications such as bearings and gears, emphasizing the superiority of transverse-oriented grooves in optimizing lubrication efficiency, extending component lifespan, and reducing friction and wear.

Supplementary Materials: The following supporting information can be downloaded at: https://www.mdpi.com/article/10.3390/lubricants13090409/s1, Figure S1: Computational process flowchart; Figure S2: Main function flowchart; Figure S3: Hertz Parameters subroutine flowchart; Figure S4: Pressure Relaxation subroutine flowchart; Figure S5: pressure iteration loop flowchart.

Author Contributions: Conceptualization, C.Y. and S.Y.; methodology, C.Y.; software, R.C. and C.M.; validation, C.Y., R.C., and C.M.; investigation, H.Z.; data curation, C.Y., R.C., and H.Z.; writing—original draft preparation, C.Y. and H.Z.; writing—review and editing, C.Y., R.C., H.Z., C.M., and S.Y.; visualization, H.Z.; supervision, C.Y.; funding acquisition, C.Y. All authors have read and agreed to the published version of the manuscript.

Funding: The authors would like to thank the funding support by the National Natural Science Foundation of China (52275184).

Data Availability Statement: The original contributions presented in this study are included in the article/Supplementary materials. Further inquiries can be directed to the corresponding author Chengjiao Yu.

Conflicts of Interest: Author Shuangcheng Yu was employed by the company Sunmetals Products of America LLC and Xingyi Metalworking Technology (Zhejiang) Co., Ltd. The remaining authors declare that the research was conducted in the absence of any commercial or financial relationships that could be construed as a potential conflict of interest.

Nomenclature

The following nomenclature are used in this manuscript:

A	The amplitude of surface topography
a_j	The amplitude of jog wave
d	The spacing of surface topography
d_x	The spacing between transversely distributed textures
d_y	The spacing between longitudinally distributed textures
E_1	Young's modulus of the ball material
E_2	Young's modulus of the substrate material
h	Local dimensional oil film thickness
H	Dimensionless oil film thickness in dimensionless computational domain
h_a	Average film thickness
h_c	Central film thickness
$h_{\max}$	Maximum film thickness

$h_{\min}$	Minimum film thickness
k_g	The wave number of the groove wave
k_j	The wave number of the jog wave
P	Dimensionless pressure in dimensionless computational domain
p_H	Maximum contact pressure in Hertzian contact
$P_{h=0}$	Dimensionless contact pressure at the position where film thickness is zero
r	The radius of surface bump
r_a	Hertzian contact radius
r_{ball}	The radius of the ball
u	Slip velocity
ν_1	Poisson's ratio of the ball material
ν_2	Poisson's ratio of the substrate material
W	Applied normal load
X, Y	The dimensionless coordinates of the computational domain
x, y, z	The dimensional coordinates of the surface
X_o, Y_o	Lower boundary in dimensionless coordinates
X_e, Y_e	Upper boundary in dimensionless coordinates
α	Pressure viscosity coefficient
β_c	Contact load ratio
$\Delta X, \Delta Y$	The grid width of the dimensionless computational domain
η	Lubrication oil viscosity
ρ	Lubricant density
Ω	The entire integral domain of the dimensionless computational domain

References

1. Guegan, J.; Kadiric, A.; Spikes, H. A Study of the Lubrication of EHL Point Contact in the Presence of Longitudinal Roughness. *Tribol. Lett.* **2015**, *59*, 22. [CrossRef]
2. Ren, N.; Zhu, D.; Chen, W.W.; Liu, Y.; Wang, Q.J. A Three-Dimensional Deterministic Model for Rough Surface Line-Contact EHL Problems. *J. Tribol.* **2008**, *131*, 011501. [CrossRef]
3. Krupka, I.; Sperka, P.; Hartl, M. Effect of surface roughness on lubricant film breakdown and transition from EHL to mixed lubrication. *Tribol. Int.* **2016**, *100*, 116–125. [CrossRef]
4. Aymard, A.; Delplanque, E.; Dalmas, D.; Scheibert, J. Designing metainterfaces with specified friction laws. *Science* **2024**, *383*, 200–204. [CrossRef]
5. Tzanakis, I.; Hadfield, M.; Thomas, B.; Noya, S.M.; Henshaw, I.; Austen, S. Future perspectives on sustainable tribology. *Renew. Sustain. Energy Rev.* **2012**, *16*, 4126–4140. [CrossRef]
6. Long, R.; Ma, Q.; Shang, Q.; Wang, H.; Yao, Y.; Wang, Y.; Zong, L. Parameter Optimization for the Improvement of Tribological Behavior of Textured Tapered Roller Bearings. *Lubricants* **2025**, *13*, 165. [CrossRef]
7. Kaneta, M.; Cameron, A. Effects of Asperities in Elastohydrodynamic Lubrication. *J. Lubr. Technol.* **1980**, *102*, 374–378. [CrossRef]
8. Choo, J.W.; Glovnea, R.P.; Olver, A.V.; Spikes, H.A. The Effects of Three-Dimensional Model Surface Roughness Features on Lubricant Film Thickness in EHL Contacts. *J. Tribol.* **2003**, *125*, 533–542. [CrossRef]
9. Zheng, C.; Yang, Y.; Cheng, S.; Wang, W.; Liu, K.; Xu, J. Friction reduction and anti-wear mechanisms of surface-textured graphite under water lubrication. *Wear* **2025**, *562–563*, 205665. [CrossRef]
10. Wang, H.-J.; Huang, J.-D.; Wang, B.; Zhang, Y.; Wang, J. Study on the Tribological Behavior of Laser Surface Texturing on Silicon Nitride Ceramic Under Water Lubrication. *Lubricants* **2025**, *13*, 21. [CrossRef]
11. Chen, X.; Huang, Y.; Rong, Y.; Wu, C. Two-step laser processing of micro/nano-composite structures on PS-SiC surfaces for superior friction performance under water-lubrication. *Ceram. Int.* **2025**, *51*, 26171–26184.
12. Jiang, S.; Liu, Q.; Ji, H.; Wang, W.; Meng, Z.; Wang, J.; Dong, G. Modeling and analysis for surface texturing on soft sliders in mixed lubrication. *Friction* **2025**, *13*, 9440917. [CrossRef]
13. Wu, Z.; Gao, L.; Huang, X.; Hua, Z. Simulation Study on the Surface Texturing Design of COC Hip Joints Based on Elastohydrodynamic Lubrication Model. *Lubricants* **2025**, *13*, 217. [CrossRef]
14. Guangteng, G.; Cann, P.M.; Olver, A.V.; Spikes, H.A. Lubricant Film Thickness in Rough Surface, Mixed Elastohydrodynamic Contact. *J. Tribol.* **1999**, *122*, 65–76. [CrossRef]
15. Patir, N.; Cheng, H.S. An Average Flow Model for Determining Effects of Three-Dimensional Roughness on Partial Hydrodynamic Lubrication. *J. Lubr. Technol.* **1978**, *100*, 12–17. [CrossRef]

16. Venner, C.H.; Lubrecht, A.A. Numerical Simulation of a Transverse Ridge in a Circular EHL Contact Under Rolling/Sliding. *J. Tribol.* **1994**, *116*, 751–761. [CrossRef]
17. Wedeven, L.D.; Cusano, C. Elastohydrodynamic Film Thickness Measurements of Artificially Produced Surface Dents and Grooves. *ASLE Trans.* **1979**, *22*, 369–381. [CrossRef]
18. Choo, J.W.; Olver, A.V.; Spikes, H.A.; Dumont, M.-L.; Ioannides, E. The Influence of Longitudinal Roughness in Thin-Film, Mixed Elastohydrodynamic Lubrication. *Tribol. Trans.* **2006**, *49*, 248–259. [CrossRef]
19. Choo, J.W.; Olver, A.V.; Spikes, H.A. The influence of transverse roughness in thin film, mixed elastohydrodynamic lubrication. *Tribol. Int.* **2007**, *40*, 220–232. [CrossRef]
20. Pei, X. Scale Effects of Surface-Texture Distribution on Lubrication and Friction. *Tribol. Lett.* **2025**, *73*, 86. [CrossRef]
21. Wang, Y.; Li, C.; Du, J.; Morina, A. Understanding the Influences of Multiscale Waviness on the Elastohydrodynamic Lubrication Performance, Part I: The Full-Film Condition. *Lubricants* **2022**, *10*, 368. [CrossRef]
22. Wang, Y.; Liu, Y. Understanding the Influences of Multiscale Waviness on the Elastohydrodynamic Lubrication Performance, Part II: The Partial-Film Condition. *Lubricants* **2024**, *12*, 190. [CrossRef]
23. Peng, F.; Jabbarzadeh, A. The Effect of Geometrical Shape of Surface Texture on the Rheology and Tribology of Confined Lubricants. *Lubricants* **2025**, *13*, 13. [CrossRef]
24. Boidi, G.; Tertuliano, I.S.; Profito, F.J.; de Rossi, W.; Machado, I.F. Effect of laser surface texturing on friction behaviour in elastohydrodynamically lubricated point contacts under different sliding-rolling conditions. *Tribol. Int.* **2020**, *149*, 105613. [CrossRef]
25. Lu, P.; Wood, R.J.K.; Gee, M.G.; Wang, L.; Pfleging, W. A Novel Surface Texture Shape for Directional Friction Control. *Tribol. Lett.* **2018**, *66*, 51. [CrossRef]
26. Choi, W.M.; Song, J.; Khang, D.-Y.; Jiang, H.; Huang, Y.Y.; Rogers, J.A. Biaxially Stretchable "Wavy" Silicon Nanomembranes. *Nano Lett.* **2007**, *7*, 1655–1663. [CrossRef]
27. Wang, Z.; Yu, C.; Wang, Q. Model for Elastohydrodynamic Lubrication of Multilayered Materials. *J. Tribol.* **2015**, *137*, 011501. [CrossRef]
28. Pu, W.; Wang, J.; Zhu, D. Progressive Mesh Densification Method for Numerical Solution of Mixed Elastohydrodynamic Lubrication. *J. Tribol.* **2015**, *138*, 021502. [CrossRef]
29. Zhu, D.; Hu, Y. The study of transition from full film elastohydrodynamic to mixed and boundary lubrication. In *The Advancing Frontier of Engineering Tribology, Proceedings of the 1999 STLE/ASME HS Cheng Tribology Surveillance*; Society of Tribologists and Lubrication Engineers: Park Ridge, IL, USA, 1999; pp. 150–156.
30. Liu, S.; Wang, Q.; Liu, G. A versatile method of discrete convolution and FFT (DC-FFT) for contact analyses. *Wear* **2000**, *243*, 101–111. [CrossRef]
31. Kaneta, M.; Sakai, T.; Nishikawa, H. Effects of Surface Roughness on Point Contact EHL. *Tribol. Trans.* **1993**, *36*, 605–612. [CrossRef]

Disclaimer/Publisher's Note: The statements, opinions and data contained in all publications are solely those of the individual author(s) and contributor(s) and not of MDPI and/or the editor(s). MDPI and/or the editor(s) disclaim responsibility for any injury to people or property resulting from any ideas, methods, instructions or products referred to in the content.